Journal of Analysis and Testing
https://doi.org/10.1007/s41664-019-00104-0

ORIGINAL PAPER

Porous Ruthenium Selenide Nanoparticle as a Peroxidase Mimic for Glucose Bioassay

Wen Cao[1,3] · Junshu Lin[1,2,3] · Faheem Muhammad[1,3] · Quan Wang[1,3] · Xiaoyu Wang[1,3] · Zhangping Lou[1,3] · Hui Wei[1,2,3]

Received: 9 April 2019 / Accepted: 3 June 2019

Abstract

Nanozyme is a promising field that offers the substitution for natural enzymes using various nanomaterials. Various nanomaterials with peroxidase-like activity were investigated. Among them, transition metal chalcogenides were explored as promising nanozymes due to their excellent enzyme-mimicking activities. However, ruthenium selenide has not been studied as a peroxidase mimic because of the difficulty for synthesis. Herein, we prepared ruthenium selenide nanomaterial with ordered mesoporous structure (P-$RuSe_2$) employing KIT-6 silica as the template. The composition and structure of P-$RuSe_2$ were fully characterized. Further, its peroxidase-like activity was investigated. P-$RuSe_2$ possessed excellent peroxidase-mimicking activity, which catalyzed the oxidation of peroxidase substrates, including 3,3′,5,5′-tetramethylbenzidine, *o*-phenylenediamine, and 2,2′-azino-bis(3-ethylbenzothiazoline-6-sulfonic acid) in the presence of H_2O_2. Moreover, P-$RuSe_2$ exhibited higher peroxidase-like activity when compared with several representative nanozymes as well as bulk $RuSe_2$. To demonstrate its potential applications, the colorimetric detection systems for H_2O_2 and glucose were successfully constructed based on P-$RuSe_2$ nanozyme.

Keywords Nanozymes · Peroxidase mimics · Artificial enzymes · Ruthenium selenide · Bionanotechnology · Glucose bioassay

1 Introduction

Enzymes have high specificity and catalytic activity under mild conditions. However, they are easy to be deactivated under harsh conditions and their production is costly, which have hindered their practical applications [1]. Therefore, artificial enzymes with higher stability and lower cost have been developed to overcome these disadvantages [2]. Among them, nanomaterials with enzyme-like activities (i.e., nanozymes) have received considerable attention recently [1, 3–22]. Till now, numerous enzymes (such as peroxidase, oxidase, catalase, superoxide dismutase, and hydrolase) have been mimicked using various nanomaterials. [1] We are particularly interested in peroxidase-like nanozymes because of their use in biosensing, biomedical imaging, therapeutics, etc., [1, 23–34]. Fe_3O_4 nanoparticles were first found to possess peroxidase-like activity [3]. Since then, various nanomaterials (such as carbon, metals, metal oxides, and transition metal chalcogenides) have been investigated to mimic peroxidases [35–40]. For example, transition metal chalcogenides (such as CuS, WS_2, NiTe, and MoS_2) have been explored as peroxidase mimics for

Wen Cao, Junshu Lin and Faheem Muhammad have equal contributions.

Electronic supplementary material The online version of this article (https://doi.org/10.1007/s41664-019-00104-0) contains supplementary material, which is available to authorized users.

✉ Hui Wei
weihui@nju.edu.cn

[1] Department of Biomedical Engineering, College of Engineering and Applied Sciences, Nanjing National Laboratory of Microstructures, Jiangsu Key Laboratory of Artificial Functional Materials, Nanjing University, Nanjing 210093, Jiangsu, China

[2] Department of Biomaterials, College of Materials, Xiamen University, Xiamen 361005, Fujian, China

[3] State Key Laboratory of Analytical Chemistry for Life Science and State Key Laboratory of Coordination Chemistry, School of Chemistry and Chemical Engineering, Nanjing University, Nanjing 210023, Jiangsu, China

Published online: 01 July 2019

H_2O_2 and glucose sensing [41–50]. Metallic ruthenium and iridium nanoparticles were also studied as peroxidase mimics, but their respective chalcogenides have yet been explored [30, 51–53]. This was partially because of the difficulty in synthesizing nanostructured ruthenium (or iridium) chalcogenides. Recently, Goodenough and co-workers prepared $RuSe_x$ nanoparticles using a supercritical-fluid (SCF) process [54]. Obviously, it is still challenging to develop a facile method to prepare ruthenium selenide nanomaterials with well-controlled morphology [55, 56]. To tackle this challenge, herein we reported the synthesis of porous $RuSe_2$ nanoparticle and investigated its peroxidase-like activity.

Many factors can affect the activity of nanozymes, such as shape, composition, surface structure, etc., [40, 57–60]. Nanozymes with larger surface areas are considered more favorable for enhancing catalytic activity because more active sites would be exposed. The porous nanostructures can provide larger surface areas compared with the corresponding bulk materials. In this regard, we envisioned that porous $RuSe_2$ nanoparticles may possess higher peroxidase-like activity.

Hard template synthesis is a well-known strategy to produce porous nanomaterials with large surface area and uniform pore distribution. In this work, we chose cubic *Ia3d* mesoporous silica KIT-6 as a hard template to produce $RuSe_2$ material with 3D ordered porous network structure (P-$RuSe_2$). We showed that P-$RuSe_2$ possessed excellent peroxidase-mimicking activity, which was then used for sensing of glucose with the combination of glucose oxidase (GOx).

2 Experimental Section

2.1 Chemicals and Materials

$RuCl_3{\cdot}xH_2O$, selenium powder, ethanol, *n*-butanol, hydrofluoric acid (40%), hydrochloric acid (37%), *o*-phenylenediamine (OPD), and polyethylene oxide–polypropylene oxide–polyethylene (PEO-PPO-PEO, P123) were purchased from Sinopharm Chemical Reagent Co., Ltd. Hydrogen peroxide (30%), tetraethyl orthosilicate (TEOS), 2,2′-azinobis(3-ethylbenzothiazoline-6-sulfonic acid) (ABTS), and 3,3′,5,5′-tetramethylbenzidine dihydrochloride (TMB) were from Aladdin Chemical Reagent Co., Ltd. All chemical reagents were utilized as received without any further purification. All aqueous solutions were prepared using deionized water (18.2 MΩ•cm, Millipore).

2.2 Instrumentation

Scanning electron microscopy (SEM) images were obtained using a Zeiss Ultra55 microscopy. Transmission electron microscopy (TEM) images were collected on a JEM-200CX microscope at an acceleration voltage of 200 kV. Powder X-ray diffraction (XRD) data was obtained on a Rigaku Ultima diffractometer. X-ray photoelectron spectroscopy (XPS) data was collected on a PHI 5000 VersaProbe electron spectrometer. UV–visible absorption spectra were recorded with a TU-1900 spectrophotometer. Nitrogen adsorption–desorption isotherm was measured using a Quantachrome Autosorb-IQ-2C-TCD-VP analyzer, and the surface area and pore size were calculated with the Brunauer–Emmett–Teller (BET) method and the Barrett-Joyner-Halenda model, respectively. Plate reader data was collected using a Tecan Infinite 200 Pro microplate reader.

2.3 Synthesis of Mesoporous KIT-6 Silica Templates

KIT-6 silica was prepared according to the previous literature. [61] Briefly, 20 g of P123 and 34 mL of HCl solution were added to 720 mL of deionized water and stirred in a polypropylene bottle. After the P123 dissolved, 20 g of *n*-butanol was added and stirred at 34 °C for 1 h. The solution was stirred at 34 °C for another 24 h after adding 43 g of TEOS. The product was collected by filtration and washed with deionized water. KIT-6 silica was obtained after calcination with 2 °C/min ramp to 550 °C for 5 h. The final product was dried overnight.

2.4 Synthesis of P-$RuSe_2$

1 g of $RuCl_3{\cdot}xH_2O$ was dissolved into 10 mL of ethanol. Then, 1 g of calcined KIT-6 template was added into $RuCl_3$ solution under stirring. The temperature of the solution was raised to 60 °C and stirred until ethanol evaporated. After loading into KIT-6 templates, the $RuCl_3$ salt was placed in one crucible, and 0.5 g selenium powder was placed in another crucible. These two crucibles were loaded into a quartz tube furnace, where the selenium powder was placed upstream. Then, the sample was heated to 550 °C at a ramp rate of 2 °C/min and maintained at 550 °C for 2 h under a forming gas of 10% H_2 in argon. Finally, P-$RuSe_2$ was obtained by removing KIT-6 silica templates with HF solution (1 M).

2.5 Synthesis of Bulk-$RuSe_2$ (B-$RuSe_2$)

B-$RuSe_2$ was obtained using the same protocol with P-$RuSe_2$ in the absence of the KIT-6 template.

2.6 Peroxidase-Like Activity Measurements

P-$RuSe_2$ nanozyme (1 mg/mL, 5 μL) was added into NaOAc–HOAc buffer (100 mM, pH 4.5) containing H_2O_2 (250 mM, 10 μL) and TMB (or OPD or ABTS) (25 mM, 10 μL). The final volume of the mixture was adjusted

to 1 mL with the buffer solution. Then, the absorption spectra of the mixture were measured with a UV–visible spectrophotometer.

2.7 H_2O_2 and Glucose Assays

H_2O_2 assay was conducted as follows. P-$RuSe_2$ nanozyme (100 μg/mL, 10 μL) was added into the buffer (70 μL, pH 4.5), then H_2O_2 with different concentrations (10 μL) and TMB (2.5 mM, 10 μL) were added. The reaction solution was well mixed immediately and then incubated at room temperature for 15 min. The absorbance at 652 nm of the reaction solution was then monitored with a microplate reader.

Glucose assay was conducted as follows. First, GOx (20 mg/mL, 10 μL) and the buffer (90 μL, pH 7.0) containing glucose with different concentrations were mixed and incubated at 37 °C for 30 min. Then, the buffer (88 μL, pH 4.5), P-$RuSe_2$ nanozyme (1 mg/mL, 2 μL) and TMB (2.5 mM, 10 μL) were added, which was incubated for another 15 min reaction. The absorbance at 652 nm of the reaction solution was then monitored with a microplate reader.

3 Results and Discussion

3.1 Characterization of P-$RuSe_2$

To verify the 3D network structure of P-$RuSe_2$, SEM imaging was employed. As shown in Fig. 1a, ordered porous structures of P-$RuSe_2$ were observed, which were composed of interconnected smaller nanoparticles. The XRD measurement was carried out to confirm the purity and phase of P-$RuSe_2$. As shown in Fig. 1b, the peaks at 30.1°, 33.7°, 37.1°, 51.0°, and 58.1° matched well with the (200), (210), (211), (311), and (321) reflections of pyrite-type $RuSe_2$ (JCPDS no. 80-0670), respectively. Note, a small peak at around 47° (as the * indicated) agreed with the crystal structure of SeO_2 (JCPDS no. 81-1001) appeared, which may be resulted from the oxidation of selenium powder during the synthesis process. To further characterize the 3D porous network morphology and crystal structure of P-$RuSe_2$, TEM imaging was carried out. TEM image (Fig. 1c) demonstrated that the porous network nanostructure was composed of spherical nanoparticles with the diameter of about 5 nm. High-resolution TEM image (Fig. 1d) revealed the highly crystalline fringes of P-$RuSe_2$.

The large surface area and high porosity are the critical feature of porous nanostructures. To study the porous nature of P-$RuSe_2$, the N_2 adsorption and desorption isotherms were measured (Fig. 2a and 2b). The BET surface area of P-$RuSe_2$ was 131.70 $m^2\ g^{-1}$, and the BJH sorption pore volume was 0.2 $cm^3\ g^{-1}$. The BET surface area of B-$RuSe_2$ was only 10.03 $m^2\ g^{-1}$ (Supplementary Fig. 1). Meanwhile, the characteristic jump attributed to the capillary condensation and the hysteresis loop of desorption curve of mesoporous structures were observed (Fig. 2a). The average pore diameter was about 6.1 nm using the BJH calculation model (Fig. 2b). The composition of P-$RuSe_2$ was investigated using XPS spectroscopy. The atomic ratio of Ru and Se was around

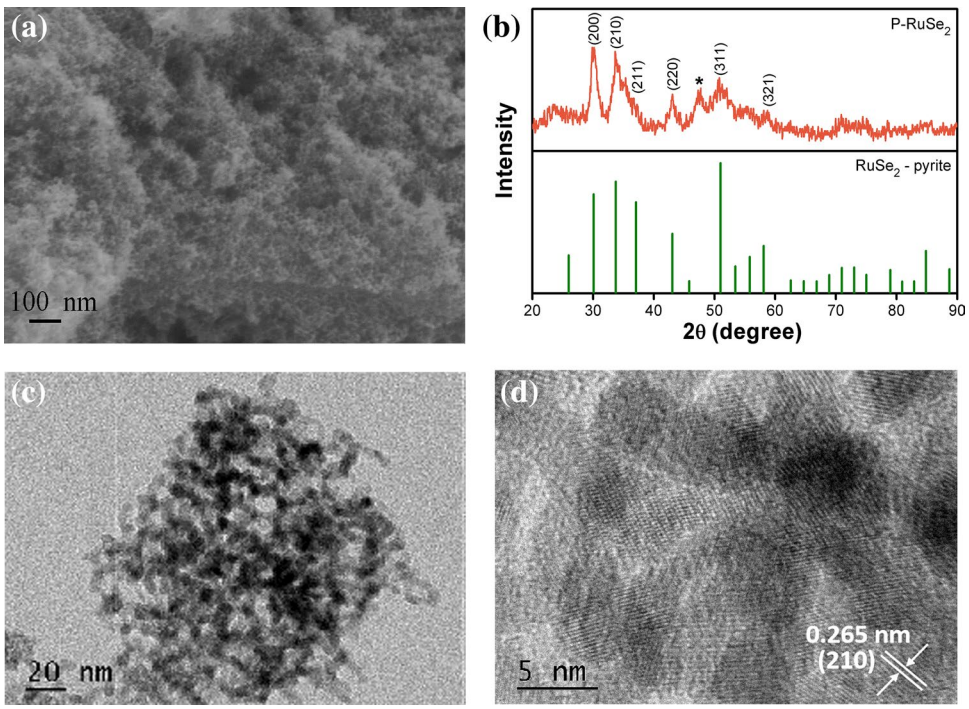

Fig. 1 **a** SEM image of P-$RuSe_2$. **b** Powder XRD patterns of P-$RuSe_2$ and pyrite-type $RuSe_2$ (JCPDS 80-0670). Low resolution (**c**) and high resolution (**d**) TEM images of P-$RuSe_2$

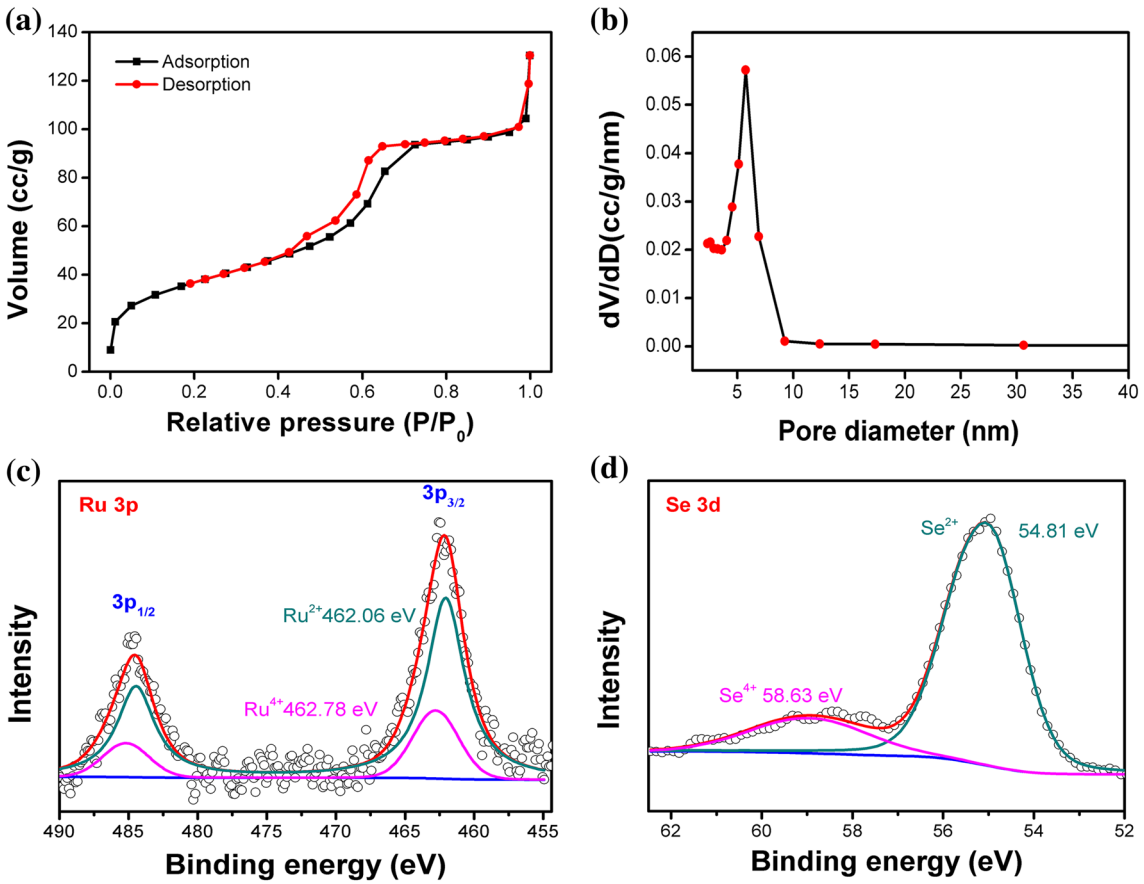

Fig. 2 **a** N_2 adsorption–desorption isotherm of P-$RuSe_2$. **b** Pore size distribution curve of P-$RuSe_2$. XPS spectra of Ru 3p (**c**) and Se 3d (**d**) of P-$RuSe_2$

1:2 according to the area integration of the peaks of Ru 3p and Se 3d, indicating the $RuSe_2$ formulation. As shown in Fig. 2c, the spectrum of Ru 3p was deconvoluted into Ru^{2+} and Ru^{4+} at 462.06 eV and 462.78 eV, respectively. Ru^{4+} was originated from $RuSe_2$, whereas Ru^{2+} could be from RuSe (Fig. 2c and Supplementary Fig. 2) [62]. The Se 3d XPS spectrum (Fig. 2d) suggested that Se 3d was mainly at 54.81 eV, which was attributed to Se^{2-}. In addition, the peak at 58.63 eV was corresponding to the oxidation-state of Se (Se^{4+}), which revealed that little selenium was oxidized during the synthesis process and agreed well with the XRD pattern. The generation of selenium oxide could not only inhibit the further growth of $RuSe_2$ nanoparticles and was beneficial to the morphology control, but could also prevent the material from oxidation by oxygen in air or solution and improve the stability of P-$RuSe_2$. [63].

3.2 Peroxidase-Like Activity

To examine the peroxidase-like activity of P-$RuSe_2$, typical colorimetric substrates of peroxidases (i.e., TMB, ABTS, and OPD) were used. As shown in Fig. 3, only the systems containing nanozyme, peroxidase substrates, and H_2O_2 produced colored products and showed obvious absorbance at 652 nm (TMBox), 418 nm (ABTSox), and 448 nm (OPDox), respectively. The result indicated that the catalytic oxidation of the substrates by P-$RuSe_2$ in the presence of H_2O_2. The nanozyme concentration-dependent activity was tested. The reaction rate increased with the increase of nanozyme concentration from 0 to 30 μg/mL (Supplementary Fig. 3a, b). Moreover, the pH- and temperature-dependent activity tests demonstrated that the optimum reaction pH and temperature were 4.5 and 60 °C, respectively (Supplementary Fig. 3c, d).

To obtain insights of the peroxidase-like activity of P-$RuSe_2$, the steady-state kinetics was investigated (Supplementary Fig. 4). With increasing the substrate concentration, the velocity increased gradually, and reached a plateau. This result showed that the nanozyme catalytic reaction obeyed the classic Michaelis–Menten kinetics. The kinetics parameters are summarized in Supplementary Table 1. The Michaelis–Menten constant (K_m) of TMB and H_2O_2 were 1.207 mM and 0.936 mM, respectively, which indicated that the affinity of P-$RuSe_2$ to H_2O_2 was higher than natural horseradish peroxidase (HRP) (3.700 mM) and the affinity to TMB was

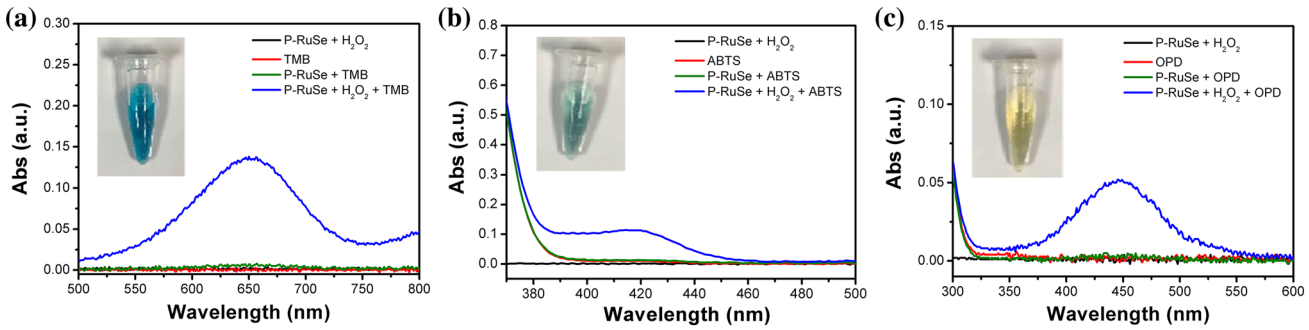

Fig. 3 Peroxidase-like activity of P-$RuSe_2$. UV–visible spectra of (**a**) TMB-H_2O_2, (**b**) ABTS-H_2O_2, and (**c**) OPD-H_2O_2 systems, respectively. Inset: the reacted solutions in presence of H_2O_2, P-$RuSe_2$, and peroxidase substrates. The concentrations of TMB, ABTS, and OPD were 0.25 mM, and the concentrations of P-$RuSe_2$ and H_2O_2 were 5 μg/mL and 2.5 mM, respectively

lower than HRP (0.434 mM). Besides, the maximum initial velocity (v_{max}) of TMB and H_2O_2 were 72.410×10^{-8} Ms^{-1} and 13.193×10^{-8} Ms^{-1}, which were larger than HRP and several representative nanozymes (Supplementary Table 1). Moreover, we have prepared bulk-$RuSe_2$ (B-$RuSe_2$), and measured its kinetic parameters for peroxidase-like activity (Supplementary Fig. 5, Supplementary Fig. 6 and Supplementary Table 1). It is clear that B-$RuSe_2$ exhibited higher v_{max} than nanozymes reported previously but lower than P-$RuSe_2$. The result indicated that porous $RuSe_2$ was more promising candidate than other compounds for peroxidase-like nanozymes and bulk $RuSe_2$.

3.3 H_2O_2 and Glucose Detection

Based on the excellent peroxidase-like activity of P-$RuSe_2$, the analytical application for detection of H_2O_2 and glucose were conducted.

Under the optimized conditions, we investigated the response to H_2O_2 at the concentration below 1000 μM. As shown in Fig. 4, two linear ranges were observed (i.e., 5−200 μM and 200−1000 μM). The relationships between UV–visible absorbance and H_2O_2 concentration were well fitted by the equations: $y=5.12\times10^{-4}x+0.07$ ($R^2=0.9975$) and $y=1.15\times10^{-4}x+0.15$ ($R^2=0.9990$) (y and x represent absorbance at 652 nm and the H_2O_2 concentration), respectively.

Then, the detection of glucose, a biologically important molecule, was carried out with the combination of GOx. Glucose was oxidized by oxygen to generate H_2O_2 in the presence of GOx. Then, the as-produced H_2O_2 reacted with the substrate TMB in the presence of P-$RuSe_2$ to produce colorimetric signals. The absorbance at 652 nm showed gradual increase with increasing glucose concentration, and reached a plateau when the concentration was higher than 2000 μM (Fig. 5a). As shown in Fig. 5b, the linear relationship between the absorbance at 652 nm and glucose concentration in the range of 5−250 μM was fitted well by the equation: $y=2.86\times10^{-4}x+0.05$ ($R^2=0.9828$) (y and x represented Absorbance at 652 nm and glucose concentration, respectively). The selectivity of the developed colorimetric assay for glucose was investigated using other sugars such as sucrose, lactose, and fructose. As shown in Fig. 5c, the other glucose analogues with a high concentration of 5 mM exhibited a negligible absorbance when compared with 1 mM glucose.

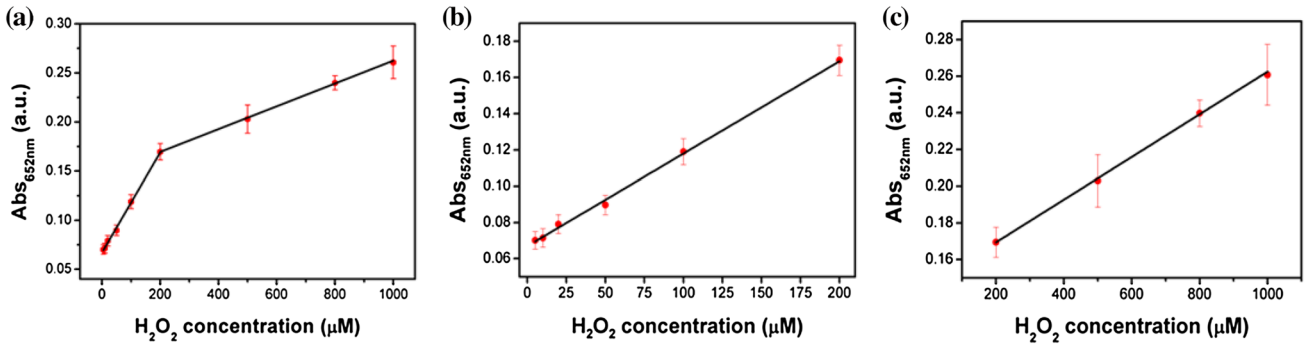

Fig. 4 **a** Plot of absorbance at 652 nm versus H_2O_2 concentration. The liner fitting in the range of 5−200 μM (**b**) and 200−1000 μM (**c**). Error bars indicate standard deviations of six independent measurements

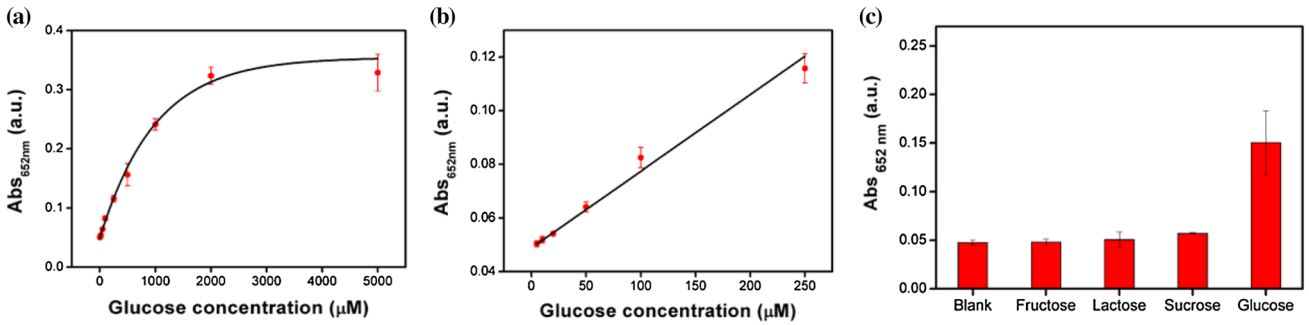

Fig. 5 **a** Plot of absorbance at 652 nm versus glucose concentration. **b** The liner fitting in the range of 5−250 μM. **c** Selectivity of glucose detection with the P-$RuSe_2$. Error bars indicate standard deviations of six independent measurements

4 Conclusions

We prepared P-$RuSe_2$ with 3D ordered mesoporous nanostructures using KIT-6 silica templates and investigated its peroxidase-like activity. The experimental results showed that $RuSe_2$ possessed better peroxidase-like activity compared with other representative nanozymes. Meanwhile, P-$RuSe_2$ showed higher peroxidase-like activity than B-$RuSe_2$, demonstrating the unique advantages of the porous nanostructure. We then used P-$RuSe_2$ nanozyme to develop the detection systems for H_2O_2 and glucose. The current study not only developed a synthetic method for P-$RuSe_2$, but also expanded the nanomaterials for peroxidase mimics.

Acknowledgements This work was supported by National Natural Science Foundation of China (21874067 and 21722503), 973 Program (2015CB659400), PAPD program, Shuangchuang Program of Jiangsu Province, Open Funds of the State Key Laboratory of Analytical Chemistry for Life Science (SKLACLS1704), Open Funds of the State Key Laboratory of Coordination Chemistry (SKLCC1819), Key Laboratory of Analytical Chemistry for Biology and Medicine (Ministry of Education) (ACBM2019001), and Fundamental Research Funds for the Central Universities (021314380145).

References

1. Wu JJX, et al. Nanomaterials with enzyme-like characteristics (nanozymes): next-generation artificial enzymes (II). Chem Soc Rev. 2019;48:1004–76.
2. Breslow R. Biomimetic chemistry and artificial enzymes: catalysis by design. Acc Chem Res. 1995;28:146–53.
3. Gao LZ, et al. Intrinsic peroxidase-like activity of ferromagnetic nanoparticles. Nat Nanotechnol. 2007;2:577–83.
4. Wei H, et al. Nanomaterials with enzyme-like characteristics (nanozymes): next-generation artificial enzymes. Chem Soc Rev. 2013;42:6060–93.
5. Zhou YB, et al. Filling in the gaps between nanozymes and enzymes: challenges and opportunities. Bioconjugate Chem. 2017;28:2903–9.
6. Lin YH, et al. Catalytically active nanomaterials: a promising candidate for artificial enzymes. Acc Chem Res. 2014;47:1097–105.
7. Zhang XZ, et al. Bioorthogonal nanozymes: progress towards therapeutic applications. Trends Chem. 2019;1:90–8.
8. Yan XY. Nanozyme: a new type of artificial enzyme. Prog Biochem Biophys. 2018;45:101–4.
9. Fan KL, et al. Magnetoferritin nanoparticles for targeting and visualizing tumour tissues. Nat Nanotechnol. 2012;7:459–64.
10. Song YJ, et al. Graphene oxide: intrinsic peroxidase catalytic activity and its application to glucose detection. Adv Mater. 2010;22:2206–10.
11. Tonga GY, et al. Supramolecular regulation of bioorthogonal catalysis in cells using nanoparticle-embedded transition metal catalysts. Nat Chem. 2015;7:597–603.
12. Natalio F, et al. Vanadium pentoxide nanoparticles mimic vanadium haloperoxidases and thwart biofilm formation. Nat Nanotechnol. 2012;7:530–5.
13. Zhang ZJ, et al. Molecular imprinting on inorganic nanozymes for hundred-fold enzyme specificity. J Am Chem Soc. 2017;139:5412–9.
14. Soh M, et al. Ceria-zirconia nanoparticles as an enhanced multi-antioxidant for sepsis treatment. Angew Chem Int Ed. 2017;56:11399–403.
15. Chen JP, et al. Rare earth nanoparticles prevent retinal degeneration induced by intracellular peroxides. Nat Nanotechnol. 2006;1:142–50.
16. Vernekar AA, et al. An antioxidant nanozyme that uncovers the cytoprotective potential of vanadia nanowires. Nat Commun. 2014;5:5301.
17. Walther R, et al. Identification and directed development of non-organic catalysts with apparent pan-enzymatic mimicry into nanozymes for efficient prodrug conversion. Angew Chem Int Ed. 2019;58:278–82.
18. Sun MZ, et al. Site-selective photoinduced cleavage and profiling of DNA by chiral semiconductor nanoparticles. Nat Chem. 2018;10:821–30.
19. Fang G, et al. Differential Pd-nanocrystal facets demonstrate distinct antibacterial activity against Gram-positive and Gram-negative bacteria. Nat Commun. 2018;9:129.
20. Shen XM, et al. Mechanisms of oxidase and superoxide dismutation-like activities of gold, silver, platinum, and palladium, and their alloys: a general way to the activation of molecular oxygen. J Am Chem Soc. 2015;137:15882–91.
21. Zhang W, et al. Prussian blue nanoparticles as multienzyme mimetics and reactive oxygen species scavengers. J Am Chem Soc. 2016;138:5860–5.
22. Xu ZB, et al. Converting organosulfur compounds to inorganic polysulfides against resistant bacterial infections. Nat Commun. 2018;9:3713.

23. Wei H, et al. Fe_3O_4 magnetic nanoparticles as peroxidase mimetics and their applications in H_2O_2 and glucose detection. Anal Chem. 2008;80:2250–4.
24. Cheng HJ, et al. Integrated nanozymes with nanoscale proximity for in vivo neurochemical monitoring in living brains. Anal Chem. 2016;88:5489–97.
25. Hu YH, et al. Surface-enhanced raman scattering active gold nanoparticles with enzyme-mimicking activities for measuring glucose and lactate in living tissues. ACS Nano. 2017;11:5558–66.
26. Wang XY, et al. Boosting the peroxidase-like activity of nanostructured nickel by inducing its 3 + oxidation state in $LaNiO_3$ perovskite and its application for biomedical assays. Theranostics. 2017;7:2277–86.
27. Cheng HJ, et al. Monitoring of heparin activity in live rats using metal-organic framework nanosheets as peroxidase mimics. Anal Chem. 2017;89:11552–9.
28. Hu YH, et al. Nitrogen-doped carbon nanomaterials as highly active and specific peroxidase mimics. Chem Mater. 2018;30:6431–9.
29. Qin L, et al. 2D-metal-organic-framework-nanozyme sensor arrays for probing phosphates and their enzymatic hydrolysis. Anal Chem. 2018;90:9983–9.
30. Wang XY, et al. Nanozyme sensor arrays for detecting versatile analytes from small molecules to proteins and cells. Anal Chem. 2018;90:11696–702.
31. Wang XY, et al. e_g occupancy as an effective descriptor for the catalytic activity of perovskite oxide-based peroxidase mimics. Nat Commun. 2019;10:704.
32. Zhang WC, et al. Pd nanoparticle-decorated graphitic C_3N_4 nanosheets with bifunctional peroxidase mimicking and ON–OFF fluorescence enable naked-eye and fluorescent dual-readout sensing of glucose. J Mater Chem B. 2019;7:233–9.
33. Kong CJ, et al. Highly-active, graphene-supported platinum catalyst for the solventless hydrosilylation of olefins. Chem Commun. 2018;54:13343–6.
34. He YF, et al. A cobalt-based polyoxometalate nanozyme with high peroxidase-mimicking activity at neutral pH for one-pot colorimetric analysis of glucose. J Mater Chem B. 2018;6:5750–5.
35. Wang JJ, et al. Polyoxometalates as peroxidase mimetics and their applications in H_2O_2 and glucose detection. Biosens Bioelectron. 2012;36:18–21.
36. Huang LJ, et al. Portable colorimetric detection of Mercury (II) based on a non-noble metal nanozyme with tunable activity. Inorg Chem. 2019;58:1638–46.
37. Shi WB, et al. Carbon nanodots as peroxidase mimetics and their applications to glucose detection. Chem Commun. 2011;47:6695–7.
38. Vernekar AA, et al. Vacancy-engineered nanoceria: enzyme mimetic hotspots for the degradation of nerve agents. Angew Chem Int Ed. 2016;55:1412–6.
39. Wang QQ, et al. GOx@ ZIF-8 (NiPd) nanoflower: an artificial enzyme system for tandem catalysis. Angew Chem Int Ed. 2017;56:16082–5.
40. Wu YH, et al. Ultra-small particles of iron oxide as peroxidase for immunohistochemical detection. Nanotechnology. 2011;22:225703.
41. Dutta AK, et al. CuS nanoparticles as a mimic peroxidase for colorimetric estimation of human blood glucose level. Talanta. 2013;107:361–7.
42. Guan JF, et al. Synthesis of copper sulfide nanorods as peroxidase mimics for colorimetric detection of hydrogen peroxide. Anal Methods. 2015;7:5454–61.
43. He WW, et al. Understanding the formation of CuS concave superstructures with peroxidase-like activity. Nanoscale. 2012;4:3501–6.
44. Lin TR, et al. Visual detection of blood glucose based on peroxidase-like activity of WS_2 nanosheets. Biosens Bioelectron. 2014;62:302–7.
45. Chen Q, et al. Hemin-functionalized WS_2 nanosheets as highly active peroxidase mimetics for label-free colorimetric detection of H_2O_2 and glucose. Analyst. 2015;140:2857–63.
46. Bai Y, et al. Novel magnetic nickel telluride nanowires decorated with thorns: synthesis and their intrinsic peroxidase-like activity for detection of glucose. Chem Commun. 2014;50:13589–91.
47. Zhao K, et al. SDS-MoS_2 nanoparticles as highly-efficient peroxidase mimetics for colorimetric detection of H_2O_2 and glucose. Talanta. 2015;141:47–52.
48. Lin TR, et al. Seeing diabetes: visual detection of glucose based on the intrinsic peroxidase-like activity of MoS_2 nanosheets. Nanoscale. 2014;6:11856–62.
49. Wang WJ, et al. Synthesis of Au-WS_2 nanocomposites and study on its peroxidase mimic activity. Chin J Anal Chem. 2018;46:1545–51.
50. Niu XH, et al. Uncapped nanobranch-based CuS clews used as an efficient peroxidase mimic enable the visual detection of hydrogen peroxide and glucose with fast response. Anal Chim Acta. 2016;947:42–9.
51. Ye HH, et al. Peroxidase-like properties of ruthenium nanoframes. Sci Bull. 2016;61:1739–45.
52. Deng HM, et al. Nanoparticulate peroxidase/catalase mimetic and its application. Chem Eur J. 2012;18:8906–11.
53. Xia XH, et al. Pd-Ir core-shell nanocubes: a type of highly efficient and versatile peroxidase mimic. ACS Nano. 2015;9:9994–10004.
54. Jang JH, et al. Superior oxygen electrocatalysis on $RuSe_x$ nanoparticles for rechargeable air cathodes. Adv Energy Mater. 2018;8:1702037.
55. Cai HY, et al. Bifacial dye-sensitized solar cells with enhanced rear efficiency and power output. Nanoscale. 2014;6:15127–33.
56. Li PJ, et al. Counter electrodes from binary ruthenium selenide alloys for dye-sensitized solar cells. J Power Sources. 2014;271:108–13.
57. Guo YJ, et al. Hemin-graphene hybrid nanosheets with intrinsic peroxidase-like activity for label-free colorimetric detection of single-nucleotide polymorphism. ACS Nano. 2011;5:1282–90.
58. Chaudhari KN, et al. Peroxidase mimic activity of hematite iron oxides (α-Fe_2O_3) with different nanostructures. Catal Sci Technol. 2012;2:119–24.
59. Liu BW, et al. Accelerating peroxidase mimicking nanozymes using DNA. Nanoscale. 2015;7:13831–5.
60. Zhang XQ, et al. Prussian blue modified iron oxide magnetic nanoparticles and their high peroxidase-like activity. J Mater Chem. 2010;20:5110–6.
61. Kleitz F, et al. Cubic Ia3d large mesoporous silica: synthesis and replication to platinum nanowires, carbon nanorods and carbon nanotubes. Chem Commun. 2003;17:2136–7.
62. Shen J, et al. An ESCA study of the interaction of oxygen with the surface of ruthenium. Appl Surf Sci. 1991;51:47–60.
63. Li HY, et al. Simple microwave preparation of high activity Se-rich $CoSe_2$/C for oxygen reduction reaction. Electrochim Acta. 2014;138:232–9.